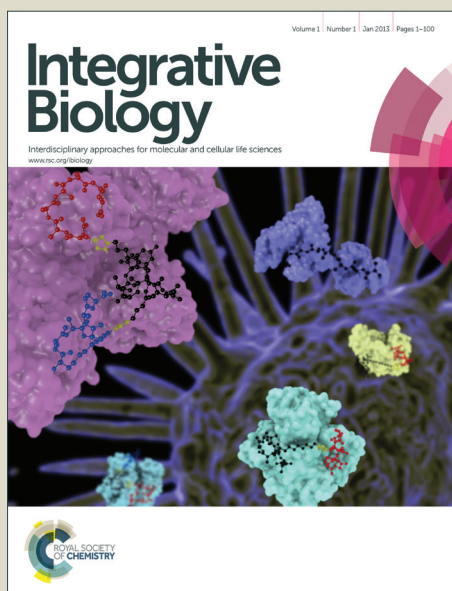


# Integrative Biology

Accepted Manuscript



This is an *Accepted Manuscript*, which has been through the Royal Society of Chemistry peer review process and has been accepted for publication.

*Accepted Manuscripts* are published online shortly after acceptance, before technical editing, formatting and proof reading. Using this free service, authors can make their results available to the community, in citable form, before we publish the edited article. We will replace this *Accepted Manuscript* with the edited and formatted *Advance Article* as soon as it is available.

You can find more information about *Accepted Manuscripts* in the [Information for Authors](#).

Please note that technical editing may introduce minor changes to the text and/or graphics, which may alter content. The journal's standard [Terms & Conditions](#) and the [Ethical guidelines](#) still apply. In no event shall the Royal Society of Chemistry be held responsible for any errors or omissions in this *Accepted Manuscript* or any consequences arising from the use of any information it contains.

Insight, innovation, integration

The ultimate challenge of systems microscopy is to provide detailed understanding of cell signalling and function. However, various cellular systems, for example the immune system are refractory to many transgene delivery methods essential for time-lapse microscopy, while existing imaging approaches provide only relative quantification. Here a flexible lentiviral gene transfer platform has been used in conjunction with a novel single-cell correlation spectroscopy analysis pipeline, to achieve for the first time, absolute quantification of temporally-resolved time-series imaging data. This showed that dynamic responses of key inflammatory networks were heterogeneously encoded in single cells, and partly dependent on morphology. This platform is suitable for future quantitative analyses of interacting signalling systems and gene transcription and ultimately better integration with mathematical models.

## ARTICLE

## Quantitative dynamic imaging of immune cell signalling using lentiviral gene transfer

Cite this: DOI: 10.1039/x0xx00000x

J. Bagnall\*, C. Boddington\*, J. Boyd\*, R. Brignall, W. Rowe, N.A. Jones, L. Schmidt, D.G. Spiller, M.R.H. White, P. Paszek

Received 00th January 2012,  
Accepted 00th January 2012

DOI: 10.1039/x0xx00000x

[www.rsc.org/](http://www.rsc.org/)

Live-cell imaging of fluorescent fusion proteins has transformed our understanding of mammalian cell signalling and function. However, some cellular systems such as immune cells are unsuitable or refractory to many existing transgene delivery methods thus limiting systematic analyses. Here, a flexible lentiviral gene transfer platform for dynamic time-lapse imaging has been developed and validated with single-molecule spectroscopy, mathematical modelling and transcriptomics and used for analysis of a set of inflammation-related signalling networks. Time-lapse imaging of Nuclear Factor kappa B (NF- $\kappa$ B), Signal Transducer and Activator of Transcription (STATs) and Nuclear Factor of Activated T-cells (NFAT) in mammalian immune cell lines provided evidence for heterogeneous temporal encoding of inflammatory signals. In particular, the absolute quantification of single-cell responses over time via Fluorescent Correlation Spectroscopy (FCS) showed that NF- $\kappa$ B p65 activation in response to Tumour Necrosis Factor  $\alpha$  (TNF $\alpha$ ) was differentially encoded in variable amplitude of nuclear translocation between immune and non-immune cells. The absolute number of activated molecules was dictated in part by the cell size, suggesting a morphology-dependent regulatory mechanism. The developed platform will enable further absolute quantitative analyses of the dynamic interactions between signalling networks, in and between individual cells, allowing better integration with mathematical models of signalling networks.

### Introduction

Regulation of cell signalling and function is a complex and dynamic process. In the immune system this process defines key gene expression signatures required for homeostasis as well as responses to infection, and is coordinated by a set of temporarily resolved transcriptional networks<sup>1</sup>. Traditional biochemical approaches are often not appropriate for their analyses, because seemingly identical cells can often display heterogeneous responses<sup>2</sup>. Live-cell imaging has contributed more toward quantitative understanding of dynamic signalling networks and cellular responses than any other technique<sup>3,4</sup>. Applications of live-cell microscopy usually depend on genetically engineered systems for expression of fluorescent protein fusions in cells. Many such systems exist, including cDNA plasmids and Bacterial Artificial Chromosomes<sup>5</sup> as well as recent genome editing technologies<sup>6,7,8</sup>. These methods vary in their ability to provide contextual transgene expression (limited by integration site and the extent of preservation of cis-acting regulatory motifs<sup>9</sup>) as well as design flexibility and targeting efficiency. While live-cell imaging of mammalian cells has become routine over recent years, many cellular systems (for example the immune system<sup>10</sup>) are refractory to existing transgene delivery methods. This is due to dependence on

inefficient chemical or electro-permeabilisation-based delivery<sup>11,12</sup>, which also limits applications of new genome editing technologies<sup>13</sup>. Viral transduction can successfully deliver transgenes<sup>10</sup> but has generally been used on a gene-by-gene basis<sup>14,15</sup> with some studies suggesting potential artefacts<sup>16</sup>.

Previous analyses highlighted the complexity of single-cell responses encoded in heterogeneous dynamics, for example, spatio-temporal pulses or oscillations in protein level or cellular localization<sup>2</sup>. In immune regulation, signalling of the Nuclear Factor kappa B (NF- $\kappa$ B) transcription factor has been thought to be particularly relevant for its dynamic single cell responses<sup>17</sup>. Tumour necrosis factor  $\alpha$  (TNF $\alpha$ )-induced oscillations in NF- $\kappa$ B p65 were shown to control downstream gene expression patterns<sup>18,19</sup>, and to encode all-or-nothing responses to varying concentration of the stimulus<sup>20,21,22</sup>. Other immune-relevant systems including Hypoxia-induced factor 1 $\alpha$  (HIF-1 $\alpha$ ), Nuclear Factor of Activated T-cells (NFAT) or Signal Transducer and Activator of Transcription (STATs) have also been shown to exhibit stimulus-induced activation dynamics. The mechanisms underlying the responses have been suggested to differ<sup>23,24,25</sup>. Surprisingly, despite the wealth of literature on NFAT signalling including *in vivo* imaging<sup>26</sup>, very few analyses exist in immune-relevant systems<sup>27</sup>.

Absolute quantification of biological phenomena has been at the forefront of systems biology, providing a better understanding of underlying processes, more statistical power for correlative analyses and ultimately allowing more accurate mathematical models to be built<sup>4</sup>. While several approaches exist (for example for analysis of gene expression<sup>28</sup>), single-cell absolute quantification methods so far have been mainly limited to static measurements of RNA<sup>29</sup> and protein levels<sup>30</sup>. Of those, the single molecule correlation spectroscopy (FCS) was shown to be particularly useful for absolute quantification of fluorescently-labelled transgenes for live-cell imaging<sup>9</sup>. Here we describe a generic platform for live-cell dynamic imaging (including difficult to target immune cells) based on lentiviral gene transfer, which provides an absolute quantification of processes involved in cell signalling, communication and fate.

## Materials and methods

### Reagents

Tissue culture medium was purchased from Gibco. MethoCult H4100™ (Stemcell Technologies) was used for imaging cells in 3D, by mixing a cell suspension with methylcellulose at a ratio of ~3:1. Cells were stimulated with Dimethylxylglycine (0.5 mM; Sigma Aldrich), LipidA Salmonella Minnesota Re595 (500 ng/ml; VWR), recombinant human and mouse TNF $\alpha$  (Calbiochem), recombinant mouse interferon- $\gamma$  (Life Technologies), phorbol 12-myristate 13-acetate (Sigma Aldrich) or Ionomycin (Sigma Aldrich).

### Cell Culture

RAW264.7 murine macrophages, immortalized mouse embryonic fibroblasts and Human Embryonic Kidney 293T cells were cultured in Dulbecco's Modified Eagle Medium supplemented with 10% foetal bovine serum (Gibco) and 1% non-essential amino acids (Sigma Aldrich). Other cell lines were cultured in RPMI 1640 supplemented with 10% foetal bovine serum. Adherent cells were sub-cultured at densities between 80-90%. Jurkat A3 cells were maintained at concentrations between  $2 \times 10^5$  and  $2 \times 10^6$  per ml.

### Western Blotting

Cells were lysed with 250  $\mu$ l Lysis buffer (1% (w/v) SDS, 10% (v/v) glycerol, 10% (v/v)  $\beta$ -ME, 8% (v/v) 0.5M Tris pH6.8, 0.01% (w/v) bromophenol blue). 18  $\mu$ l samples and 8  $\mu$ l of ladder (NEB #P7712S, USA) were loaded onto gels. Proteins were transferred to nitrocellulose membranes (Optitran BA-S85, Schleicher & Schuell) incubated at room temperature in blocking buffer (5% (w/v) non-fat milk powder in TBS-T), washed in TBS-T and incubated overnight with RelA (p65) primary antibody (Cell Signalling #8242) at 1:1000 dilution in blocking buffer. Membranes were washed (TBS-T x3), and incubated with 1:2000 HRP-conjugated IgG (Cell Signalling #7074) for 2 hours. Membranes incubated for 5 min with 5 ml chemiluminescent Luminata™ Crescendo Western HRP Substrate (EMD Millipore Corp.). Luminescence was captured using a Bio-Rad Gel Doc XRS+ System.

## Introduction of Gateway Cassette to Lentiviral Vectors

The N-terminal fusion vector was generated by restriction digestion of pG-EGFP-B plasmid using XbaI and AscI enzymes, then ligating the fragment into lentiviral FUGW backbone<sup>31</sup> (a gift from David Baltimore; Addgene plasmid #14883). The C-terminal fusion vector was generated by restriction digest of pG-C-EGFP using AscI and AgeI enzymes, and ligation into FUGW plasmid. The IRES2 vector was cloned by restriction digest of pG-IRES2-EGFP with the enzymes AscI and AgeI, and ligation into FUGW. The resulting vectors were named pLNT-UbC-EGFP-#, pLNT-UbC-#-EGFP and pLNT-UbC-#-IRES2-EGFP respectively (where # denotes the gateway recombination insertion site).

### Switching reporter genes

The EGFP reporter was replaced in the N- and C- fusion vectors by a series of reporter gene sequences, including tagBFP, AmCyan, mVenus, tagRFP, mCherry, mKate2, Dendra2 and a FLAG-tag. For the N-terminal fusion vector (pLNT-UbC-EGFP-#) first the reporter gene in the pG-EGFP-B vector was replaced using the restriction enzymes AgeI and XhoI. Then, the resulting pG-'newreporter'-B vector was digested by XbaI and AscI and the fragment ligated into pLNT-UbC-EGFP-#. The EGFP sequence in the pLNT-UbC-#-EGFP was replaced with a new reporter gene by restriction digest with AgeI and AscI. The list of cloning primers is available in *Electronic Supplementary Information*.

### Propagation and cloning with Gateway Lentiviral Vectors

All pLNT destination vectors carry the ampicillin antibiotic resistance and must be propagated in ccdB resistant bacteria as per the standard Gateway protocols (available on the Life Technologies website). Terminal (post-recombination) destination vectors were propagated in Subcloning Efficiency DH5a cells (Life Technologies) and grown on ampicillin Luria-broth agar plates (50 $\mu$ g/ml).

### Cloning target sequences into pLNT vectors

Target sequences were amplified by PCR using primers that carry the necessary recombination sequences (see *Electronic Supplementary Information*). The HIF-1 $\alpha$ , NF- $\kappa$ B1 and p50 murine sequences were amplified from cDNA from the RAW264.7 cell line. Human p65 was amplified from p65-dsRedxp plasmid<sup>19</sup>. Murine p65 was amplified from RelA cFlag pcDNA3 plasmid<sup>32</sup> (a gift from Stephen Smale, Addgene plasmid 20012). Murine STAT1 was amplified from the I.M.A.G.E consortium plasmid (IRAV8D07). Human NFATc2 was synthesised with flanking recombination sequences, then inserted into the puc57 vector (GenScript). All amplified genes were transferred to the pLNT destination vectors using the standard Gateway cloning protocols. Briefly, this involves a recombination to introduce the sequence into the Gateway® pDONR/zeo entry vector (Life Technologies), followed by a recombination to transfer the gene to a pLNT expression vector.

### Lentivirus Production

$1.25 \times 10^7$  HEK293T cells were seeded into a 15cm dish and transfected by polyethylenimine "Max" (Polysciences, inc.) with 10.5 $\mu$ g total DNA made up by the packaging vectors pMDLg-RRE, pCMV-VSVG, pRSV-REV and the pLNT transfer vector at a 2:1:2:4 ratio. After 6 h the transfection mix was removed and replaced with fresh media. After 48 h, the media was collected and the virus concentrated by ultracentrifugation at 100,000 G for 90 minutes<sup>33</sup>. The virus was resuspended in 100  $\mu$ l of 1xPBS, which has been measured to produce titres of  $1 \times 10^7$  TU/ml<sup>33</sup>. The virus was either freshly applied to cells or frozen at -80°C for future use.

### Cell Transduction

Cell cultures of  $1.5 \times 10^4$  cells in 2 ml were incubated for 2 days in the presence of between 50 to 100  $\mu$ l of the lentiviral preparation. Multiple transductions of a cell line were carried out sequentially, leaving a minimum of 3 days between repeat transductions. Transduction efficiency was determined by confocal microscopy.

### Transient transfection

Transient transfection was performed with Fugene6 (Promega). Cells were plated in 35 mm dishes in culture medium prior to transfection. The transfection mix was made as according to manufacturers instructions using a Fugene6-to-DNA ( $\mu$ l: $\mu$ g) ratio of 4:2 for MEF cells and 2:1 for SK-N-AS cells.

### Confocal Microscopy

Cells were plated onto 35 mm-glass bottomed dishes (Greiner Bio-One) (using Corning® Cell-Tak™ adhesive for Jurkat cells). Cells were then incubated on the microscope stage at 37°C in humidified 5% CO<sub>2</sub>. Zeiss confocal microscopes were used (LSM Pascal, Exciter, 510meta, 710 or 780), which used either dichroic mirrors and band-pass filters or spectral separation or detector arrays to collect appropriate emission signals following excitation of the fluorophore with the appropriate laser. Image capture was performed using the Zeiss software, either "Aim version 4.2 utilizing the Autofocus macro<sup>34</sup>" on the 5-series microscopes or "Zen 2010b SP1" on the 7-series microscopes. A range of objectives, as appropriate for the cell type, were also employed for all imaging, Fluar 20x NA 0.75 (air), Fluar 40x NA 1.3 (oil immersion), and plan-apochromat 63x NA 1.4 and 100x NA 1.46 (oil immersion).

### Image Analysis

Cell Tracker (version 0.6) was used to quantify time-lapse confocal images<sup>35,36</sup>. The data was exported as mean fluorescence intensity. Volume measurements were made using Z-stack images in Imaris software (Bitplane).

### RNA sequencing

Total RNA was extracted from RAW264.7 cells by using the Roche High Pure RNA Isolation Kit. RNA sequencing (RNA-seq) libraries were generated using the TruSeq® Stranded mRNA assay (Illumina, Inc.) according to the manufacturer's

protocol. Briefly, total RNA (0.1-4  $\mu$ g) was used as input material from which polyadenylated mRNA was purified using poly-T, oligo-attached, magnetic beads. The mRNA was then fragmented using divalent cations under elevated temperature and then reverse transcribed into first strand cDNA using random primers. Second strand cDNA was then synthesized using DNA Polymerase I and RNase H. Following a single 'A' base addition, adapters were ligated to the cDNA fragments, and the products then purified and enriched by PCR to create the final cDNA library. Adapter indices were used to multiplex libraries, which were pooled prior to cluster generation using a cBot instrument. The loaded flow-cell was then paired-end sequenced (100 + 100 cycles, plus indices) on an Illumina HiSeq2500 instrument. Demultiplexing of the output data (allowing one mismatch) and BCL-to-Fastq conversion was performed with CASAVA 1.8.3. Sequencing data is available from ArrayExpress under accession no E-MTAB-3155.

### Analysis of RNA-sequencing data

Paired reads were mapped to the mouse genome assembly GRCm38.p3 (ENSEMBL<sup>37</sup>) using TopHat<sup>38</sup>. Aligned reads were mapped to genomic features (Mus\_musculus.GRCm38.75.gff) using the read summarization software featureCounts<sup>39</sup> within the subread package. Differential expression between cell lines was performed with a paired experimental design using edgeR<sup>40</sup>. A 1% false discovery rate (FDR) cut-off was used to establish significant differences. Gene ontology enrichments were determined using DAVID<sup>41</sup>. REVIGO software package was used for visualization, where closely related GO-terms are clustered together within a tree-map where the size of the rectangles is proportional to the enrichment of those terms<sup>42</sup>. All differentially expressed genes were clustered in terms of median log<sub>2</sub> fold changes across replicates (treated/untreated) and visualized as a heat map.

### Fluorescence Correlation Spectroscopy

FCS was carried using either a Zeiss LSM780 or Zeiss LSM710 with confocor 3 mounted on an Axio observer Z1 microscope using either a fluar 40x NA 1.3, plan-apochromat 63x NA 1.4, or plan-apochromat 100x NA 1.46 oil immersion lens. EGFP fluorescence was excited by 488 nm laser light and emission collected between 500 and 530 nm, and dsRedxp and TagRFP were excited by 561 nm laser light and emission collected between 580 and 630 nm after passing through a pinhole set to one Airy unit. Laser power was typically <1% total power, but was adjusted as necessary to avoid photo-bleaching and also to give a suitable count rate with a minimum 0.5kHz counts per molecule. The protocols as outlined in Kim et al.<sup>30</sup> were followed with either 10 x 10 second runs used for each measurement, or 5 x 5 second runs used for more motile cells. Zen 2010B software was used for data collection, with a binning time of 200 ns. A custom made script for FCS data fitting was written in MATLAB R2014b (Mathworks) using the Optimisation Toolbox based on the Marquardt-Levenberg algorithm.

In a correlation spectroscopy experiment, the normalized correlation curve of the fluorescent signal  $F(t)$ , is defined as

$$G(\tau) = \frac{\langle F(t+\tau) \cdot F(t) \rangle}{\langle F(t) \rangle^2} - 1, \quad \tau \geq 0,$$

where  $\tau$  represents the lag time, and  $\langle \cdot \rangle$  denotes averaging over time. For each measured point, the corresponding autocorrelation curve was fitted using a previously described approach for live cells<sup>43</sup>, with one non-fluorescent process and two diffusing components of different sizes allowed as follows

$$G(\tau) = \frac{1}{N(1-T)} \cdot \left[ 1 - T \cdot \left( 1 - e^{-\frac{\tau}{T}} \right) \right] \cdot \sum_{i=1}^2 \left[ a_i \cdot \left( 1 + \frac{\tau}{\tau_{D_i}} \right)^{-1} \cdot \left( 1 + \frac{\tau}{\tau_{D_i} \cdot S^2} \right)^{-\frac{1}{2}} \right].$$

Here  $N = c \cdot V_{eff}$  is the average number of fluorescent molecules in the confocal volume  $V_{eff}$  and  $c$  their concentration,  $T$  represents the non-fluorescent component due to transitions of the fluorescent molecules into the triplet state,  $a_i$  is the relative fraction of each diffusive species, and  $S = Z_0/W_0$  is the structural parameter which depends on the observation volume, with  $Z_0$  being the axial and  $W_0$  the lateral dimension of the confocal volume. The characteristic diffusion time(s)  $\tau_D$  is related to the diffusion coefficient  $D$  and is given by  $D = W_0^2/4\tau_D$ . Diffusion times and concentrations were extracted after calibrating the confocal volume  $V_{eff} = \pi^{3/2}W_0^3S$  by estimating  $W_0$  and  $S$  using Rhodamine 6G with known<sup>44</sup> diffusion constant of  $400 \mu\text{m}^2\text{s}^{-1}$ . The confocal volume was estimated to be approximately  $0.57 \pm 0.11$  fL agreeing with previous measurements<sup>45</sup> (see *Electronic Supplementary Information*, Fig. S8A). Autocorrelation curves were used to calculate counts per second per molecule (molecular brightness), allowing for relative comparison between free and fused fluorophore for experiments carried out under the same conditions on the same day. For this comparison, MEF:Gp65 cells were compared to cells transiently expressing the pLNT-Ubc-EGFP-p65 vector or pEGFP-N1 vector (Clontech).

### Quantified Time-Lapse Imaging

Prior to performing a time-lapse confocal experiment, FCS measurements were performed in the cytoplasm for one to five cells per imaging location yielding a range of molecule concentrations (per confocal volume) across several cells. These were compared to the average fluorescence intensities from a corresponding confocal slice at the FCS spot positions revealing a linear relationship between concentration and intensity. Intensities were averaged locally by taking a five-pixel radius circle after background intensity, measured in an area with no cells for each imaging location, had been subtracted. The same microscope configuration was used for both FCS measurements and confocal imaging, although a linear increase in measured molecule number was confirmed for pinhole sizes of 1-3 Airy units (Fig. S9). FCS-measured concentration distribution was also used to calibrate additional data sets by quantile-quantile matching to the respective

fluorescence distribution; thereby the cells can be quantitatively imaged on microscopes without FCS capability (Fig. S17).

### Mathematical processing of imaging time-series data

The mean-normalized raw imaging data were represented as a time-series  $X=(X_1, X_2, \dots, X_N)$ ,  $Y=(Y_1, Y_2, \dots, Y_N)$ , where  $X$  and  $Y$  corresponded to measured signals and  $N$  was the number of temporal measurements. Using a sliding window of length  $K$ , the cross-correlation coefficient  $R_i^K(x_i, y_i)$ , where  $x_i=(X_{i-K/2}, \dots, X_{i+K/2})$  and  $y_i=(Y_{i-K/2}, \dots, Y_{i+K/2})$  for  $i=K/2, K/2+1, \dots, N-K/2$  was calculated as

$$R_i^K(x_i, y_i) = \sum_{j=1}^K [(x_i(j) - \mu_x)(y_i(j) - \mu_y)],$$

where  $\mu_x$  and  $\mu_y$  were means of  $x_i$  and  $y_i$  respectively (for each sequence normalised so the auto-correlation was equal to 1).

We aimed to detect regions that showed a high correlation between time-series  $X$  and  $Y$  (the protein fusion of interest, and the nuclear marker H2B, respectively). A window length of 26 data points was chosen, such that the correlation coefficient  $>0.4$  was statistically significant at the p-value of 0.05 (Fig. S5A). For statistical detection of correlation coefficients  $<0.4$ , longer window lengths are required, which would limit the locality of the analysis.

The average correlation coefficient ( $R_{ave}$ ) for the entire time-series ( $X, Y$ ) was then calculated as

$$R_{ave}(X, Y) = \frac{\sum_{i=1}^{N-K} R_i^K(x, y)}{(N-K)},$$

where  $N-K$  was the total number of local correlation coefficients. Similarly, the local coefficient of variation was calculated as

$$Cv_i = \frac{\sigma_{x_i}}{\mu_{x_i}},$$

where  $\sigma_{x_i}$  was the sample standard deviation of  $x_i$ . In addition, the average coefficient of variation was also calculated

$$Cv_{ave}(X, Y) = \frac{\sum_{i=1}^K Cv_i^2(x, y)}{(N-K)}.$$

In order to remove local correlations from the measured time-series data, three nonlinear regression models were constructed to fit the nuclear marker trace,  $m$ , to the raw fusion trace of interest,  $p$ :

$$\text{M1: } p(t) = p^*(t) + \beta \cdot m(t) + \gamma,$$

$$\text{M2: } p(t) = \alpha \cdot m(t) \cdot p(t) + p^*(t) + \beta \cdot m(t) + \gamma,$$

$$\text{M3: } p(t) = \alpha \cdot m(t)^2 p(t) + p^*(t) + \beta \cdot m(t) + \gamma,$$

where  $\alpha, \beta$  and  $\gamma$  were constant parameters to be fitted and  $p^*$  was the residual from the fitted trace. Protein traces,  $p_i$ , were then inferred from each of the models as

$$p_1(t) = p^*(t),$$

$$p_2(t) = \alpha \cdot m(t) \cdot p(t),$$

$$p_3(t) = \alpha \cdot m(t)^2 \cdot p(t).$$

The protein trace  $p_i$  that minimised average cross-correlation  $R_{ave}(m, p_i)$  was then chosen as the inferred protein fusion trace. For the inferred protein fusion trace  $p_i$  peak detection, baseline correction and area-under-curve analysis was performed using Prism software (GraphPad Prism version 6.00 for Windows, GraphPad Software, San Diego California USA). Peaks detected that spanned the full length of the time-series, were less than 2 data points or identified at the start or end of the time-course were ignored.

## Results

### Gateway Lentiviral Platform for live-cell imaging

In order to successfully deliver relevant transgene reporter constructs into cells, a set of novel recombination-mediated transfer vectors were developed, which were compatible with a third generation lentiviral expression system<sup>46</sup>. This was achieved using an existing ubiquitin ligase C-driven (UbC) lentiviral expression vector<sup>31</sup> that was modified to include Gateway (Invitrogen) recombination cassettes<sup>47</sup> in three different orientations. This enabled the possibility of N- and C- terminal tagging as well as split-fusions via the IRES2 sequence. With the Gateway recombination system, any sequence of interest may be efficiently transferred into an appropriately tagged vector, which can then be used for lentiviral transduction (see *Materials and Methods*). In order to maximize the capacity for multi-parameter imaging we included a comprehensive set of fluorescent fusion proteins covering a palette of colours from the blue to far-red of the visible spectrum (Fig. 1A). This theoretically enables simultaneous imaging of four different signals with AmCyan, Venus, tagRFP and mKate2 fusions<sup>48</sup>. In addition we included photo-convertible Dendra2 and photo-switchable Dronpa, which can be used to determine protein half-lives or import/export rates in subcellular compartments, respectively<sup>49,50</sup>. We also incorporated a FLAG-tag for use with biochemical purification or precipitation techniques<sup>51</sup>. Overall, this system provides a highly flexible platform for engineering fusion expression vectors, which in combination with lentiviral delivery is applicable to a wide range of cell types.

Here, in order to demonstrate the generic nature of the lentiviral platform, and its suitability for imaging single-cell temporal dynamic

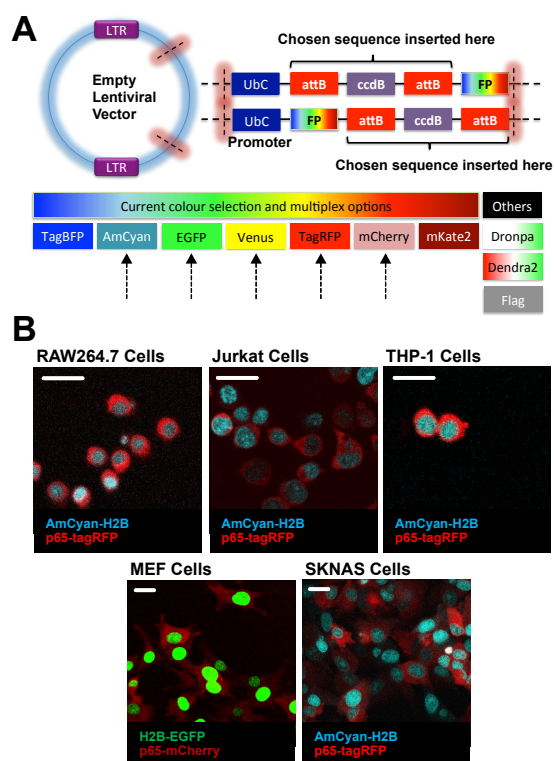


Fig 1. (A) Schematic of the recombination-mediated lentiviral transfer vectors available. The black arrows indicate the reporter genes used within this manuscript, while the remaining vectors are a part of the developed system. (B) Confocal images of developed cell lines for NF- $\kappa$ B p65 signaling. Shown are RAW264.7:p65R, Jurkat:p65R, THP1:p65R, MEF:p65M and SKNAS:p65R cells. Scale bar denotes 20 $\mu$ m.

| Cell line            | Transgenes                              | Construct                  | Species                    |
|----------------------|---|----------------------------|----------------------------|
| RAW264.7:p65R        | AmCyan-H2B<br>p65-tagRFP                | pLNT                       | mouse macrophage           |
| RAW264.7:HIF1aV-p65R | AmCyan-H2B<br>p65-tagRFP<br>HIF1a-Venus | pLNT                       | mouse macrophage           |
| RAW264.7:STAT1G      | AmCyan-H2B<br>STAT1-EGFP                | pLNT                       | mouse macrophage           |
| RAW264.7:Vp50        | Venus-p50                               | pLNT                       | mouse macrophage           |
| RAW264.7:Vp105       | Venus-p105                              | pLNT                       | mouse macrophage           |
| RAW264.7:Gp65        | EGFP-p65                                | (Tay <i>et al.</i> , 2010) | mouse macrophage           |
| Jurkat:VNFATc2       | Venus-NFATc2                            | pLNT                       | human T cell               |
| Jurkat:p65R          | AmCyan-H2B<br>p65-tagRFP                | pLNT                       | human T cell               |
| THP1:p65R            | AmCyan-H2B<br>p65-tagRFP                | pLNT                       | human monocyte             |
| SKNAS:p65R           | AmCyan-H2B<br>p65-tagRFP                | pLNT                       | human neuroblastoma        |
| MEF:Gp65             | EGFP-p65                                | (Tay <i>et al.</i> , 2010) | mouse embryonic fibroblast |
| MEF:p65M             | H2B-EGFP<br>p65-mCherry                 | pLNT                       | mouse embryonic fibroblast |

Table 1. List of Cell Lines used with corresponding expressed transgenes

signalling, it has been used to characterize several immune-relevant transcription factors. We transformed a number of immune cell lines (mouse macrophage RAW264.7 and human T-cell Jurkat) to stably

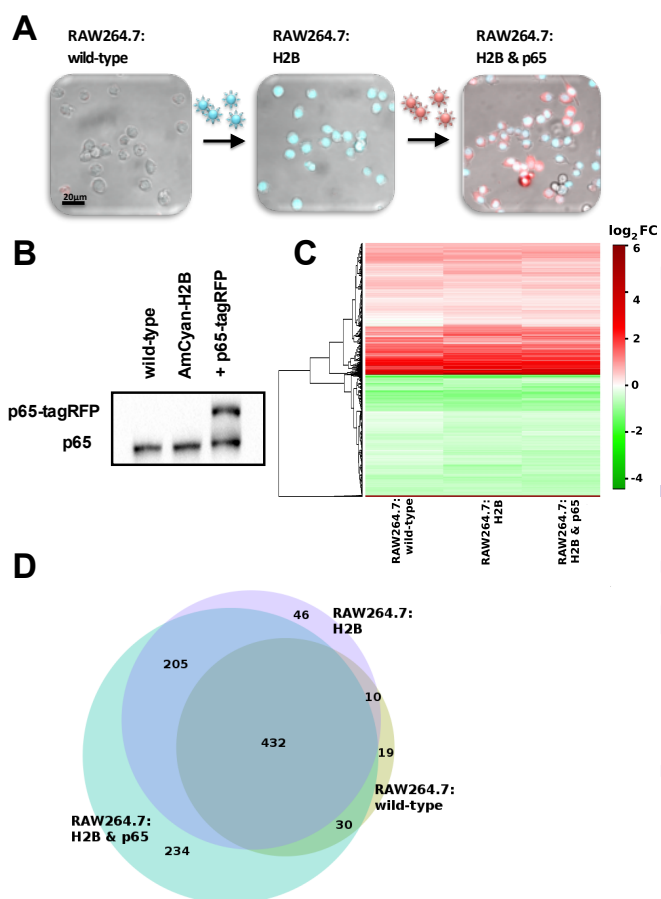


Fig 2. (A) Engineering of AmCyan-H2B and p65-tagRFP transduced RAW264.7 cells. (B) Immunoblotting analysis of NF- $\kappa$ B p65 protein expression level in wild type (WT), AmCyan-H2B, and AmCyan-H2B and p65-tagRFP (+p65-tagRFP) transduced RAW264.7 cells. (C) Gene expression patterns of cell lines from A after 3h stimulation with 500ng/ml of Lipid A. Differentially expressed genes were clustered in terms of median log2 fold changes across replicates (stimulated/unstimulated control) and visualized as a heat map. (D) Venn diagram of Lipid A-regulated genes from C.

express fluorescent HIF-1 $\alpha$ , STAT1, NFATc2 as well as components of the NF- $\kappa$ B family, namely p65, NF $\kappa$ B1 and p50. In order to aid with automated analysis of time-lapse images<sup>35,36</sup> and processing of time-series data, these cell lines also expressed a nuclear H2B protein fusion (Fig. 1B for NF- $\kappa$ B p65 system, Table 1).

We first tested the lentiviral delivery in RAW264.7 macrophages using a previously characterized bacterial endotoxin model<sup>27,52</sup>. Cells were sequentially transduced with AmCyan-H2B then NF- $\kappa$ B p65-tagRFP transgenes with a produced viral titre (Fig. 2A). Stable cell lines were established with 98% and 92% of cells fluorescent for AmCyan-H2B and p65-tagRFP, respectively (Fig. S1). Analysis of wild type (WT), AmCyan-H2B transduced and dual AmCyan-H2B and p65-tagRFP transduced cells (+p65-tagRFP) by Western blot suggested that the protein expression of endogenous NF- $\kappa$ B p65 was not affected (Fig. 2B). Also, in the same cells, the level of transduced p65-tagRFP appeared to be similar to that of endogenous NF- $\kappa$ B p65 protein. The NF- $\kappa$ B system is involved in transcriptional regulation of hundreds of genes, which are critical for the inflammatory response<sup>53,54</sup>. Lentiviral delivery of exogenous NF- $\kappa$ B p65 (and H2B) was compared to untransformed wild-type (WT) RAW264.7 cells. The transcriptomes of unstimulated WT, AmCyan-H2B and dual AmCyan-H2B and p65-tagRFP RAW264.7 macrophages differed in the induction of only 11 genes (out of approximately 11k expressed genes) after AmCyan-H2B transduction and a further induction of 41 genes (notably a 2-fold increase of NF- $\kappa$ B p65 expression consistent with protein data in Fig. 2D, Fig. S2) after p65-tagRFP transduction (see *Supplementary*

*Data*). Cell lines were then stimulated for 3h with 500 ng/ml of Lipid A (the principal cytotoxic component of the lipopolysaccharide of the gram-negative bacteria<sup>52</sup>) and differential expression analysis between cell lines was performed (see *Materials and Methods*). A robust Lipid A-stimulated gene expression pattern (981 genes across different cell lines) was consistent with a pro-inflammatory signature. This included a number of cytokines (e.g., TNF $\alpha$ , interleukin 1 $\alpha$ , 1 $\beta$ , 10, 15, 27), chemokines (e.g., CCL2, 3, 5, 6, 9, 22 and Cxcl2, 10, 11, 16) and other inflammatory mediators (see Fig. S3 and *Supplementary Data* for gene ontology analysis). A comparison between cell lines showed that gene expression patterns were not qualitatively affected by either the AmCyan-H2B or the NF- $\kappa$ B p65-tagRFP transduction (as shown by clustering analysis, Fig. 2C and overlapping Venn diagram, Fig. 2D). These analyses indicated that despite NF- $\kappa$ B p65's role as a critical regulator of the response to endotoxin physiological gene expression patterns were maintained in response to lentiviral transduction.

### NF- $\kappa$ B, STAT, HIF and NFAT signalling in immune-cells

In order to demonstrate the generic applicability of the lentiviral platform, we systematically quantified single-cell responses in RAW264.7 macrophages and Jurkat T-cells with respect to a number of inflammation-related signalling systems (Fig. 3A). In hypoxia, hydroxylase inhibition increases HIF-1 $\alpha$  protein half-life and

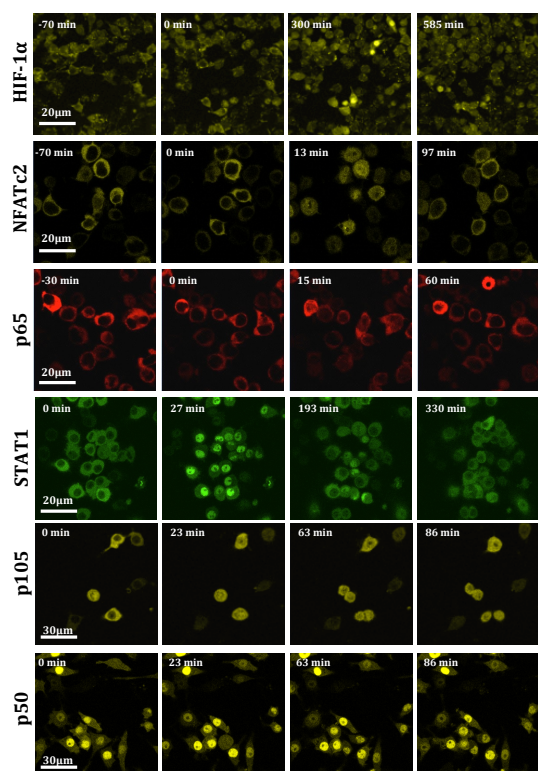


Fig 3: Time-lapse confocal images of RAW264.7 and Jurkat cells expressing various fluorescent fusion proteins: RAW264.7:HIF1 $\alpha$ V cells stimulated with 0.5 mM dimethylxalylglycine, Jurkat:VNFATc2 cells stimulated with 1 $\mu$ g/ml ionomycin and 20 ng/ml PMA, Jurkat:p65R cells stimulated with 30 ng/ml of TNF $\alpha$ , RAW264.7:STAT1G cells stimulated with 100 ng/mlIFN $\gamma$ , RAW264.7:Vp105 cells stimulated with 500 ng/ml LipidA, RAW264.7:Vp50 cells stimulated with 500ng/ml LipidA.

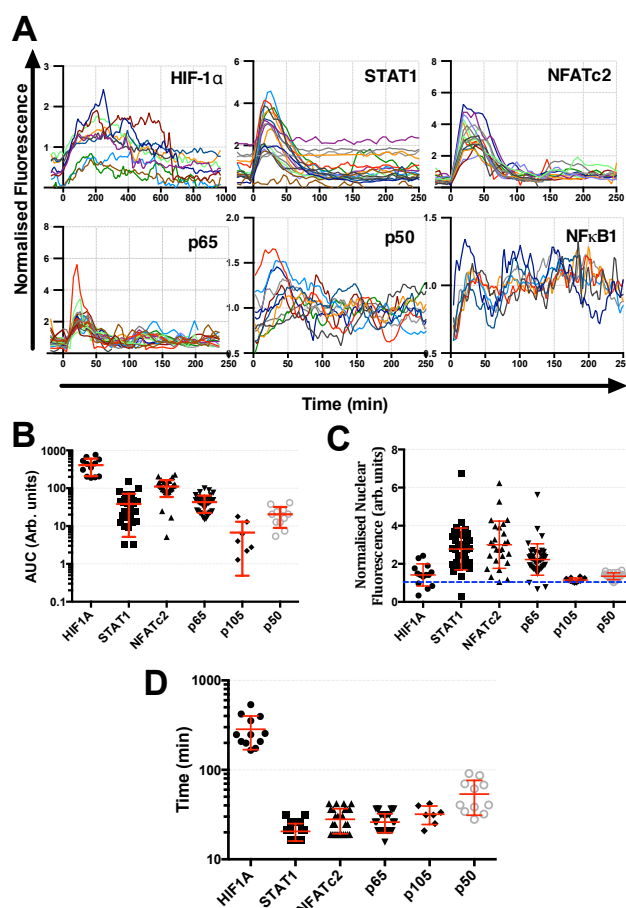


Fig 4: (A) Processed single-cell traces of data in Fig. 3. (B) Area under curve analysis for data in A. (C) Amplitude of first peak for data in A, with a blue dashed line to indicate average initial normalised value of 1. (D) Time to first peak for data in A.

induces its nuclear accumulation<sup>23</sup>. In RAW264.7 macrophages HIF-1 $\alpha$  exhibited a single nuclear translocation in response to 0.5 mM of hydroxylase inhibitor dimethylxalylglycine, however the peak timing and the level of translocation in individual cells was variable. STAT1 and NFATc2 also exhibited a single phase of nuclear translocation lasting up to 2 h in response to interferon- $\gamma$  (IFN $\gamma$ ) stimulation in RAW264.7 cells, and phorbol 12-myristate 13-acetate (PMA) and ionomycin stimulation in Jurkat cells, respectively. However, the STAT1 and NFATc2 responses were much more rapid (in comparison to HIF-1 $\alpha$ ) and lasted for about 100 min, suggesting an acute regulatory feedback<sup>24,25</sup>. Also a rapid single nuclear translocation of NF- $\kappa$ B p65 was observed in response to 30 ng/ml of TNF $\alpha$  in Jurkat T-cells. In contrast, previous single-cell analyses in non-immune cell types showed more persistent oscillatory p65 responses to TNF $\alpha$ <sup>20,18</sup>. Heterogeneous oscillatory dynamics were exhibited by NF- $\kappa$ B p105 and its proteolytically processed inhibitory subunit p50 in response to LipidA stimulation (Fig. 4A) in RAW264.7 macrophages, suggesting a tighter temporal control in those cells<sup>17</sup>. Stimuli-specific single immune cell responses

exhibited substantial cell-to-cell heterogeneity in terms of activation level (Fig. 4B-C), and timing (Fig. 4D), reflecting diverse regulatory mechanisms<sup>23,24,25</sup>. These signalling pathways often function as an interconnected network sharing common target genes<sup>17</sup>. Therefore, it would be of interest to investigate how their respective temporal responses integrate. Overall, these data highlighted the complexity and heterogeneity of inflammatory signalling, and reinforced the need for more quantitative single-cell analyses to resolve the origin and function of these responses.

### Mathematical analysis of single-cell imaging data

In order to quantify a number of parameters encoded in single cell responses such as the timing and integral of nuclear translocations<sup>20,18,55</sup> we developed a post-processing algorithm that uses a nuclear H2B protein (or any alternative nuclear marker) signal as a reference to identify cell movement fluctuations or aid with interpretation of morphological changes (Fig. 5A, see *Materials and Methods*).

An example “raw” trajectory of Lipid A-stimulated RAW264.7 macrophage cell showed a number of noisy nuclear translocations of the NF- $\kappa$ B p65-tagRFP and a variable AmCyan-H2B nuclear marker signal (Fig. 5B). Cell movement artefacts were observed around 800min post-stimulation, as indicated by the rapid fluctuations in the nuclear level of p65-tagRFP and AmCyan-H2B signals (Fig. 5C). Consequently, a high negative correlation between the two signals was detected around 800 min (Fig. 5D). We used regression analysis to infer nuclear p65-tagRFP time-series (with three regression models  $p_i$ ,  $i=1,2,3$ ) based on the measured H2B signal (Fig. S5B). The high negative correlation was successfully removed by model  $p_1$  and  $p_2$  (but not  $p_3$ ) without affecting uncorrelated regions (Fig. 5D), while reducing signals’ variability (measured by local coefficient of variation, Fig. S5C). Model  $p_2$  minimized the correlation with the H2B signal (measured by average cross correlation  $R_{ave}=0.1$  vs. 0.22 and 0.26, Fig. S5D), and thus was used as an inferred p65-tagRFP time-series in subsequent analyses (Fig. 5C).

We applied the post-processing algorithm to four single-cell datasets in RAW264.7 macrophages transduced with either p65-EGFP or STAT1-EGFP (and the AmCyan-H2B). Cells were stimulated with 30 ng/ml and 1 ng/ml of TNF $\alpha$  as well as 10 ng/ml and 1 ng/ml of IFN $\gamma$ , respectively (see Fig. S6 for a heat map of individual traces). Individual regression models performed differently against the data with some time-series well represented by the raw traces (Fig. S6). However, peak detection comparison with the processed traces (Fig. S7) showed a reduced number of responding cells to low dose stimulations (Fig. 5E). Also, the area under the response curve corresponding to nuclear NF- $\kappa$ B p65 and STAT1 translocation was reduced in the processed data (Fig. 5F), providing a better quantitative interpretation of the observed single-cell responses.

### Absolute quantification of transgene expression by FCS

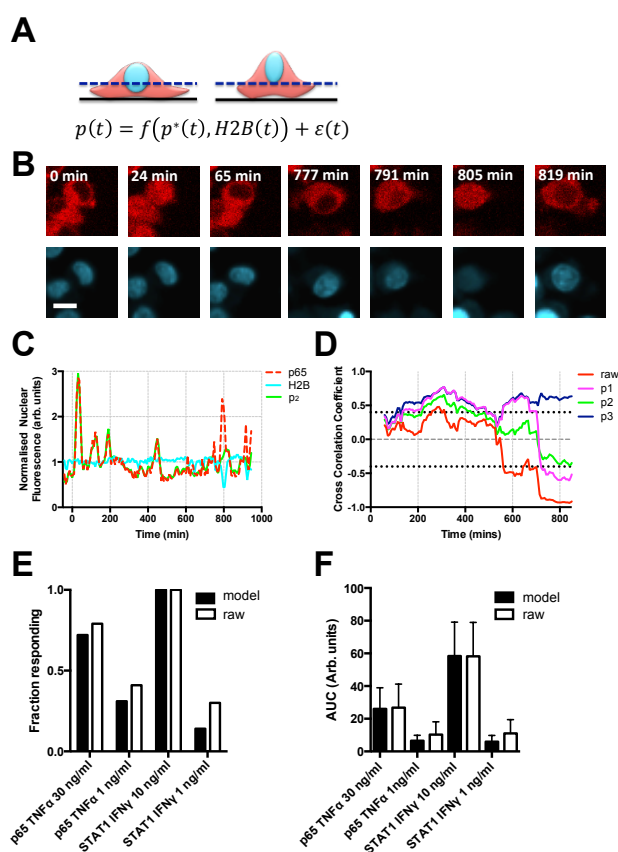


Fig. 5: Mathematical analysis of dynamic inflammatory signaling in single-cells. (A) Schematic representation of the processing algorithm: Artifacts of a cell moving in and out of the focal plane (dashed line) were removed by regression analysis. The observed protein trace,  $p$ , is a function of nuclear concentration,  $p^*$ , cell movement (as measured by H2B signal) and measurement noise. (B) Time-lapse confocal images of RAW264.7 AmCyan-H2B (cyan) and p65-tagRFP cell (red) stimulated with 500 ng/ml Lipid A. Scale bar represents 10  $\mu$ m. (C) Time course of mean normalized nuclear p65-tagRFP (red), AmCyan-H2B (green) of data in B.  $P_2$  is the inferred protein trace from time series regression analysis. (D) Time course of cross correlation coefficients between raw AmCyan-H2B, p65-tagRFP nuclear trace and fitted traces (models  $p_1$ ,  $p_2$ ,  $p_3$ ). (E) Stacked bar chart of responding cells in raw and inferred p65-EGFP and STAT1-EGFP traces in RAW264.7 stimulated with 30ng/ml and 1ng/ml of TNF $\alpha$  as well as 10ng/ml and 1ng/ml of IFN $\gamma$ , respectively, data from Figure S17. (F) Area under curve analysis of first peak nuclear translocation in raw and modeled data from E.

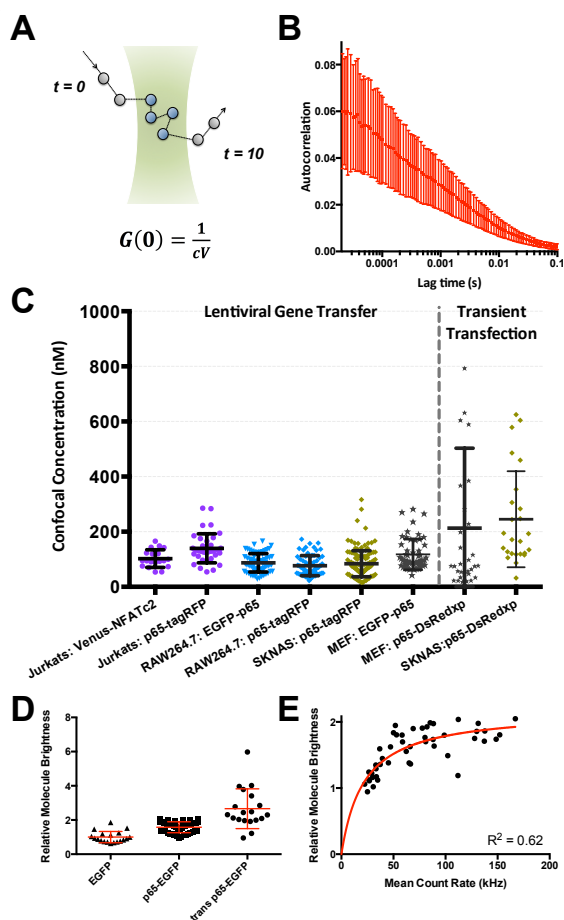


Fig 6: FCS quantification of transgene expression and time-lapse imaging. (A) Schematic representation of FCS analysis: the amplitude  $G(0)$  of the autocorrelation function is inversely proportional to the number of fluorescent molecules in the confocal volume. (B) Autocorrelation curve for a single experiment with RAW264.7:p65R cells (mean and standard deviation of 66 cells). (C) Confocal concentration measurements of transgene protein fusion expression. Data collected in Jurkat:VNFATc2 (19 cells), Jurkat:p65R (37), RAW264.7:p65R (69), RAW264.7:p65R (66), MEF:Gp65 (55) and SKNAS:p65R (119) as well as SKNAS (25) and MEFs (31) transiently transfected with p65-DsRedXP construct. Shown are individual cell confocal concentrations (nM), as well as means and standard deviations. (D) Relative molecular brightness of EGFP-p65 protein under stable ( $n=47$  cells) and transient ( $n=19$  cells) expression, compared to transient expression of free EGFP ( $n=19$  cells) in MEFs. (E) Further analysis of relative molecular brightness of MEF:Gp65, against mean photon count rate. Red line shows a saturation binding curve fit.

Fluorescent Correlation Spectroscopy (FCS) allows the determination of the number and concentration of fluorescently labelled molecules in living cells by autocorrelation analysis of the intensity fluctuations over time (Fig. 6A). The amplitude of the autocorrelation function is inversely proportional to the number of fluorescent molecules in the small confocal volume (Fig. 6B for an average autocorrelation curve for a single experiment with 66 RAW264.7:p65R cells, Fig. S9 for individual cells). FCS was used to compare fluorescent-fusion protein expression levels in hundreds of cells from transformed cell lines expressing different constructs. Concentrations were calculated based on the FCS measurement in a confocal volume in the cytoplasm ( $0.57 \text{ fL} \pm 0.11$  as determined using known concentrations of rhodamine6G in solution, Fig. S8A). The measurement yielded approximately  $76 \text{ nM} (\pm 37)$  of NF- $\kappa$ B p65-tagRFP in RAW264.7: p65R cells (Fig. 6C). This was used as a baseline for further comparisons. The same pLNT Ubc-promoter-driven p65-tagRFP construct stably expressed in Jurkat cells showed somewhat higher cytoplasmic concentration of  $140 \text{ nM} (\pm 53)$ , whilst the cytoplasmic concentration of Venus-NFATc2 was  $102 \text{ nM} (\pm 32)$ .

Another lentiviral NF- $\kappa$ B p65-EGFP vector driven by a proximal p65 promoter<sup>20</sup> showed a similar  $87 \text{ nM} (\pm 33)$  transgene protein concentration in RAW264.7 macrophages in comparison with the Ubc promoter-driven pLNT system developed here. We then used human-S-type neuroblastoma (SK-N-AS) and mouse embryonic fibroblast (MEFs) cells<sup>18</sup> in order to enable comparison between lentiviral and transient transfection delivery methods. SKNAS:p65R and MEF:Gp65 cells transduced with p65-tagRFP and EGFP-p65 expressed  $84 \text{ nM} (\pm 47)$  and  $118 \text{ nM} (\pm 56)$  of protein fusion, respectively. In contrast, when transiently transfected with p65-DsRedxp construct (in wild-type SKNAS and MEFs) the respective average concentrations were much higher, and exhibited large heterogeneity between individual cells,  $212 \text{ nM} (\pm 290)$  and  $245 \text{ nM} (\pm 174)$ , respectively.

Overall, this analysis showed that the lentiviral gene delivery provided low and homogenous (in comparison with transient transfection) transgene expression of approximately  $100 \text{ nM}$  over a range of cell lines, transgenes, promoters or fusion proteins.

One potential factor affecting the FCS quantification could be oligomerization of protein fusions. We attempted to measure this for NF- $\kappa$ B p65 protein, which forms homo- or heterodimeric complexes<sup>56</sup>. First, we measured the molecular brightness of free EGFP transiently transfected into MEFs, taken to be in a monomeric state<sup>43</sup> (Fig S11). In comparison, the transiently expressed EGFP-p65 showed a relative molecular brightness of  $2 (\pm 1.1)$ , indicating a high degree of p65 dimerization in all cells (Figure 6D). In contrast, the relative molecular brightness in lentivirally-derived MEF:Gp65 cells was equal to  $1.58 (\pm 0.3)$ . Relationship between measured fluorescence levels and relative molecular brightness suggested that dimerization of EGFP-p65 in MEF:Gp65 cells depended on the expression level of the fusion protein (Figure 6E). This analysis suggested that lentivirally transduced EGFP-p65 was (on average equally) distributed between hetero and homodimeric states, whereas transient transfection resulted in a dimeric state. This analysis allow interpreting our FCS measurement as a quantification of an ‘functional’ number of molecules, e.g., in the case of NF- $\kappa$ B p65 a number of homo- or heterodimers containing at least one p65 fusion protein. In this case, the number of total NF- $\kappa$ B p65 per cells molecules would be on average larger than the FCS-estimate by around 30%. This analysis provides further evidence that the lentiviral system provides a more physiological transgene expression levels (comparing to transient expression).

#### Relationship between cell size and NF- $\kappa$ B p65 protein level

We analysed absolute NF- $\kappa$ B p65-tagRFP expression levels in RAW264.7:p65R macrophages (that were used in transcriptomics analysis, Fig. 2) by simultaneous FCS and 3D volume measurements in single cells suspended in methylcellulose (Fig. 7A). Measurements gave an average cytoplasmic volume of  $553 \text{ fL} \pm 222$  in RAW264.7 cells (and  $850 \text{ fL} \pm 574$  in MEFs for comparison) (Fig. 7B, see also Fig. S12 for total volumes). FCS measurements showed that in the cytoplasm of individual cells there were on average  $13.8 \pm 7.6$  “functional” molecules/dimers of p65-tagRFP in the confocal volume (Fig. S13). This was lower than the equivalent measurement

of  $26.0 \pm 12.5$  dimers in adherent RAW264.7 cells, suggesting that FCS in suspended cells was compromised by the larger distance from the objective to the point of interest. There was no correlation between the concentration of fluorescent molecules in individual cells and the corresponding cell volume (Fig. 7C, Fig. S15), indicating that the total number of molecules scaled with cell size, which proved to be the case (Fig. 7D). The estimation of total cytoplasmic expression of  $60000 \pm 50000$  dimers of EGFP-p65 in MEFs (Fig. S14 and Fig. S15) from adherent cells were considered to be more accurate, which was in good agreement with previous mathematical models of the NF- $\kappa$ B system which assumed  $10^5$  p65 molecules per cell<sup>20,57</sup>. The number of p65 fusion containing dimers estimated in RAW264.7 cells was lower ( $25000 \pm 6000$  molecules), partially reflecting the relative size of those cells (Fig. 6B).

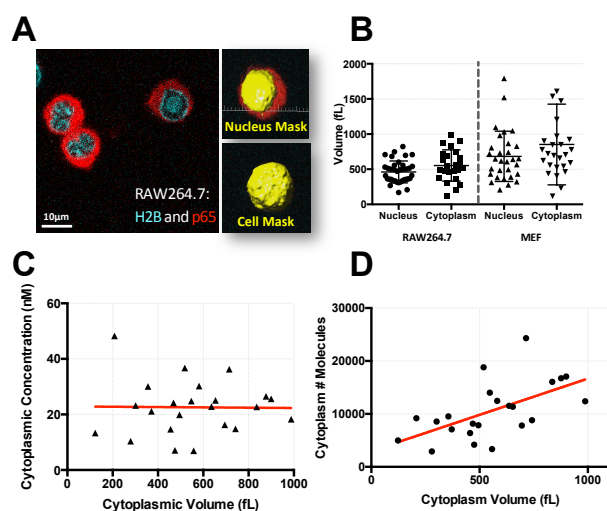


Fig 7. (A) Schematic representation of the simultaneous 3D FCS and volume estimation for RAW264.7:p65R cells suspended in methylcellulose. (B) 3D nuclear and cytoplasmic volume measurements in RAW264.7:p65R and MEF:Gp65 cells, 38 and 30 cells, respectively. (C) Correlation between 3D cytoplasmic concentrations (nM) and cytoplasmic volumes for RAW264.7:p65R cells in B. (D) Correlation between 3D total number of molecules and cytoplasmic volumes for RAW264.7:p65R cells in B.

### FCS-calibrated quantitative imaging of NF- $\kappa$ B p65 dynamics

The ultimate challenge of systems microscopy is to provide quantitative temporally resolved time-series data<sup>4</sup>. Historically, additional static normalization controls or mathematical modelling<sup>20,18,55</sup> provided quantitative aspects of such analyses. Here, in order to enable absolute quantification of dynamic live-cell data, we used an FCS-calibrated single-cell imaging workflow<sup>9</sup>. 2D confocal measurements were used to calibrate time-series imaging fluorescent data (Fig. 8A). We found a linear relationship between the levels of fluorescent intensity of p65-tagRFP and the FCS measurement in un-stimulated RAW264.7:p65R cells (Fig. 8B, scaling factor of  $1.48 \pm 0.1$ ). The FCS-calibrated scaling was applied and time-series fluorescent data converted into absolute concentrations (example workflow for RAW264.7:p65R cells stimulated with 100 ng/ml TNF $\alpha$  shown in Fig. 8A, see also Fig. S18A and S19A for SKNAS and MEF cells). Representative cell traces of FCS-calibrated time series data in RAW264.7:p65R after 100 ng/ml TNF $\alpha$  stimulation (as well as MEF:Gp65 and

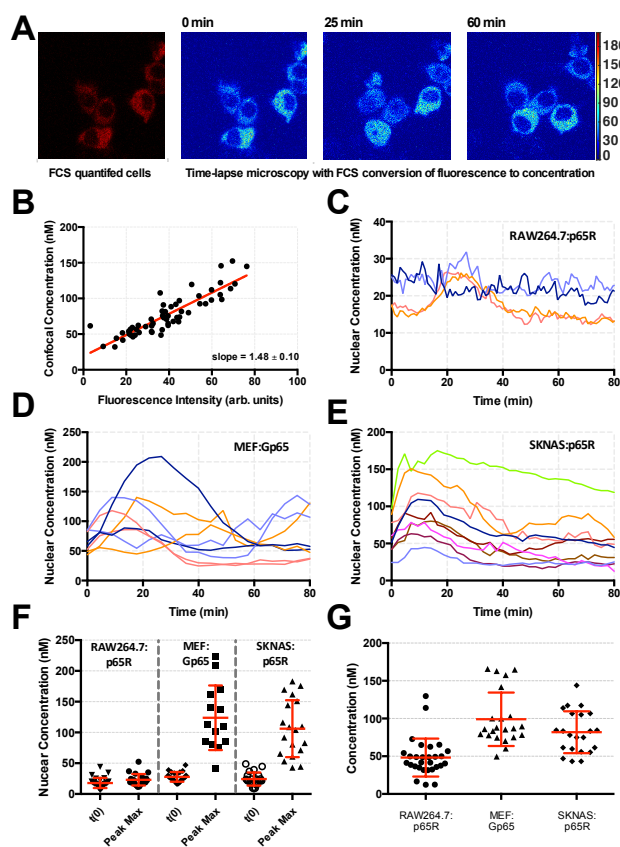


Fig 8. (A) FCS-calibrated workflow for time-lapse imaging quantification. Shown are confocal microscopy images of RAW264.7:p65R cells (left) and calibrated images following 100ng/ml TNF $\alpha$  stimulation at 0, 25 and 60mins. Scale bar represents absolute concentration in nM. (B) Correlation between 2D confocal concentrations and fluorescent intensities in 59 RAW264.7:p65R cells. A slope of regression line (in red) defined a scaling factor between the two measurements. (C) Representative cell traces of FCS-calibrated time series data in RAW264.7:p65R stimulated with 100ng/ml TNF $\alpha$ , and MEF:Gp65 (D) and SKNAS:p65R (E) cells in response to 10ng/ml TNF $\alpha$ . (F) Analysis of basal and peak nuclear NF- $\kappa$ B p65 protein fusion nuclear concentration for experiment in F-H (35, 25 and 23 cells, respectively). (G) Initial cytoplasmic concentrations of p65 across cell types.

SKNAS:p65R cells in response to 10 ng/ml TNF $\alpha$ ), exhibited nuclear translocations of NF- $\kappa$ B p65 protein (Fig. 8C-E). Comparison between cell lines showed that while the basal nuclear NF- $\kappa$ B p65 fusion levels were similar (approximately 20-30 nM), stimulated peak nuclear concentration in RAW264.7 macrophages (30 nM) was much lower than in SK-N-AS (120 nM) and MEF (150 nM) cells (Fig. 8F). Nuclear concentrations equated to a change from approximately 5000 to 6500 “functional” molecules/dimers NF- $\kappa$ B p65 in RAW264.7 cells, while MEFs exhibited a greater increase from approximately 11000 to 50000 “functional” molecules of p65 fusion on average. This was only in part reflected by basal cytoplasmic concentrations of NF- $\kappa$ B p65 fusion (two-fold difference between RAW264.7 and other cells, Fig. 8G and Fig. S20) suggesting a key TNF $\alpha$  signal transduction component. We expect that the reduced availability of the NF- $\kappa$ B p65 molecules in RAW264.7 macrophages might have substantial effect on downstream gene expression, as the number of active molecules will not likely saturate up to  $10^5$   $\kappa$ B binding sites across the genome<sup>58</sup>. Low levels and availability of NF- $\kappa$ B p65 molecules may also impact on the plethora of the reported interacting partners<sup>56</sup>. Among many other potential applications, by multiplexing with additional fluorescent gene expression reporters our FCS-calibrated imaging

workflow will be ideally suited to investigate how the different levels of nuclear NF- $\kappa$ B potentially correlate with transcription<sup>59</sup>.

## Discussion

Here we developed and validated a platform for quantitative live-cell imaging of cellular signalling networks. Our approach provides a highly flexible way of engineering fusion expression vectors, which in combination with lentiviral delivery is applicable to a wide range of cell types facilitating systematic single-cell analyses. While many other transgene delivery methods exist including recent genome-editing technologies<sup>6,7,8</sup>, which arguably provide a more contextual transgene expression<sup>9</sup>, many cellular systems are refractory to these approaches. Using single-cell fluorescence correlation spectroscopy we showed that our lentiviral system could provide near-to-physiological and relatively homogenous expression levels (in comparison with transient transfection) that were independent of cell lines, transgenes and fusion proteins used. We also suggested that viral transduction, when used as a tool for derivation of stable lines preserved contextual gene expression programs (in an important bacterial endotoxin model). Ultimately, the choice of the expression system for live cell imaging depends on the underlying biology, and may affect the utility of the analyses so caution is recommended. However, here we showed that in a set of signalling networks (especially those relying on translocation dynamics or half-life regulation<sup>2,23</sup>) a lentiviral gene transfer may be a viable (and often the only available) method for flexible engineering of model systems.

Cellular signalling is inherently a complex and dynamic process often leading to heterogeneous cell fate decisions<sup>2</sup>. A key aim of systems microscopy analyses is to provide a better understanding of cell signalling by quantitative temporally resolved time-series data. Single cell quantification has previously been achieved by static imaging measurements<sup>9,29,30</sup> or mathematical fitting of time series data<sup>20,18,55</sup>. Here we developed a FCS-calibrated time-lapse imaging approach that for the first time enabled quantification of single-cell responses over time in terms of absolute concentration or molecular numbers. Signalling molecules often exist in oligomeric functional forms (for example NF- $\kappa$ B, STAT and NFAT regulate transcription via dimeric complexes<sup>56,60,61</sup>, while p53 tumour suppressor acts as a tetramer<sup>62</sup>). The accurate estimation of total number molecules, which may exist in distributed oligomeric states poses a difficult challenge, however our approach provided a substantial step towards achieving this goal. Using a photon counting histogram (PCH) analysis<sup>63</sup>, we were able to estimate the degree of oligomerization between fusion proteins (Fig. 5) and thus interpret our FCS measurement in terms of the 'functional' number of molecules, e.g., number of different oligomers. Using the FCS quantification we calculated that in mouse fibroblast cells, the NF- $\kappa$ B nuclear translocation in response to TNF $\alpha$  equated to approximately on average 40000 p65 fusion-containing p65 dimers, however, in Raw264.7 macrophages only 1000 dimers translocated. Macrophages (but not fibroblast cells) have the ability to produce large amounts of TNF $\alpha$  in response to pathogen-

related molecular patterns<sup>64,65</sup>, therefore their lower sensitivity to TNF $\alpha$  might represent a regulatory motif, which prevents out-of-context activation and propagation of inflammation by self-perpetuating production of TNF $\alpha$  and other pro-inflammatory cytokines. FCS-calibrated live-cell imaging also showed that concentrations of signalling molecules were largely preserved across varying cell sizes (and thus cell types), and therefore the absolute number of activated molecules (e.g., level of nuclear NF- $\kappa$ B translocation) was dictated in part by the cell volumes. We hypothesise that cell morphology might constitute a rudimentary mechanism for fine-tuning cellular responses, for example during differentiation, or cell cycle processes, which involve a change of cell size<sup>66,67</sup>.

Exploiting developed tools, the behaviour of a number of inflammatory signalling networks were examined, which included NF- $\kappa$ B, HIF1 $\alpha$ , STAT1 and NFAT transcription factors in immune-relevant cell lines. Analysis of single cell responses revealed a range of heterogeneous dynamics including pulsatile and oscillatory responses, which spanned across different time scales (Figs 3 and 4). These responses exhibited differential stimulus sensitivity suggesting both digital and analogue signal processing. For example, the decrease of TNF $\alpha$  and IFN $\gamma$  dose resulted in lower fractions of responding cells as well as reduced level of activation (Fig. 5). Analysis of the NF- $\kappa$ B signalling in response to endotoxin challenge demonstrated for the first time that in addition to previously characterised p65<sup>18,27</sup>, other family members, namely p105 (and its proteolytically processed inhibitory subunit p50) also exhibited oscillatory dynamics (Fig. 5). This suggests an intriguing possibility that the regulation of the NF- $\kappa$ B-dependent gene expression might involve a number of dynamically regulated components, whose regulation has to be tightly coordinated, perhaps similar to this seen in mechanical clockworks.

In conclusion, this study reinforced the need for more quantitative single-cell analyses to resolve the origin and function of single-cell responses. The quantitative aspects of the techniques described here will in the future enable analyses of interacting signalling systems and gene transcription, and ultimately better data integration with mathematical models.

## Acknowledgements

We thank Dean Jackson and other members of Systems Microscopy Centre in Manchester for fruitful discussions and Mark Muldoon for help with modelling. We also thank Brian Bigger for providing expertise in lentiviral systems, David Baltimore, Stephen Smale, Markus Covert and Violaine Sée for providing plasmids, and Genomic Technologies Core Facility in the Faculty of Life Sciences, Manchester for assistance. PP holds a BBSRC David Phillips Research Fellowship (BB/I017976/1). CB, JB and RB are supported by BBSRC PhD studentships. This work was also supported by MRC (MR/K015885/1), BBSRC (BBF0059381, BB/K003097/1) and Wellcome Trust

(097820/Z/11/B). The work leading to these results has received funding from the European Union Seventh Framework Programme (FP7/2012-2017) under grant agreement n° 305564.

## Notes and references

<sup>a</sup> Faculty of Life Sciences, University of Manchester, AV Hill Building, Oxford Road, Manchester, M13 9PT.

email: [pawel.paszek@manchester.ac.uk](mailto:pawel.paszek@manchester.ac.uk)

\* These authors contributed equally to this work

† Electronic Supplementary Information (ESI) available: [Electronic Supplementary Information includes additional information, and Supplementary Data for gene expression analysis]. See DOI: 10.1039/b000000x/

1. J. Stark, C. Chan and A. J. George, *Immunological reviews*, 2007, **216**, 213-231.
2. J. H. Levine, Y. Lin and M. B. Elowitz, *Science*, 2013, **342**, 1193-1200.
3. D. Muzzey and A. van Oudenaarden, *Annual review of cell and developmental biology*, 2009, **25**, 301-327.
4. D. G. Spiller, C. D. Wood, D. A. Rand and M. R. White, *Nature*, 2010, **465**, 736-745.
5. I. Poser, M. Sarov, J. R. Hutchins, J. K. Hérliche, Y. Toyoda, A. Pozniakovskiy, D. Weigl, A. Nitzsche, B. Hegemann, A. W. Bird, L. Pelletier, R. Kittler, S. Hua, R. Naumann, M. Augsburg, M. M. Sykora, H. Hofemeister, Y. Zhang, K. Nasmyth, K. P. White, S. Dietzel, K. Mechtler, R. Durbin, A. F. Stewart, J. M. Peters, F. Buchholz and A. A. Hyman, *Nature methods*, 2008, **5**, 409-415.
6. M. Bibikova, K. Beumer, J. K. Trautman and D. Carroll, *Science*, 2003, **300**, 764.
7. J. Boch, *Nature biotechnology*, 2011, **29**, 135-136.
8. B. Chen, L. A. Gilbert, B. A. Cimini, J. Schnitzbauer, W. Zhang, G. W. Li, J. Park, E. H. Blackburn, J. S. Weissman, L. S. Qi and B. Huang, *Cell*, 2013, **155**, 1479-1491.
9. R. Mahen, B. Koch, M. Wachsmuth, A. Z. Politi, A. Perez-Gonzalez, J. Mergenthaler, Y. Cai and J. Ellenberg, *Molecular biology of the cell*, 2014, **25**, 3610-3618.
10. S. Froelich, A. Tai and P. Wang, *Immunopharmacology and immunotoxicology*, 2010, **32**, 208-218.
11. C. K. Payne, *Nanomedicine*, 2007, **2**, 847-860.
12. S. Wang and L. J. Lee, *Biomicrofluidics*, 2013, **7**, 11301.
13. H. Koike-Yusa, Y. Li, E. P. Tan, C. Velasco-Herrera Mdel and K. Yusa, *Nature biotechnology*, 2014, **32**, 267-273.
14. E. Warlich, J. Kuehle, T. Cantz, M. H. Brugman, T. Maetzig, M. Galla, A. A. Filipczyk, S. Halle, H. Klump, H. R. Scholer, C. Baum, T. Schroeder and A. Schambach, *Molecular therapy : the journal of the American Society of Gene Therapy*, 2011, **19**, 782-789.
15. N. Krupka, P. Strappe, J. Gotz and L. M. Ittner, *Plasmid*, 2010, **63**, 155-160.
16. A. Follenzi, L. Santambrogio and A. Annoni, *Current gene therapy*, 2007, **7**, 306-315.
17. M. S. Hayden and S. Ghosh, *Genes & development*, 2012, **26**, 203-234.
18. L. Ashall, C. A. Horton, D. E. Nelson, P. Paszek, C. V. Harper, K. Sillitoe, S. Ryan, D. G. Spiller, J. F. Unitt, D. S. Broomhead, D. B. Kell, D. A. Rand, V. See and M. R. White, *Science*, 2009, **324**, 242-246.
19. D. E. Nelson, A. E. C. Ihekweaba, M. Elliott, J. R. Johnson, C. A. Gibney, B. E. Foreman, G. Nelson, V. See, C. A. Horton, D. G. Spiller, S. W. Edwards, H. P. McDowell, J. F. Unitt, E. Sullivan, R. Grimley, N. Benson, D. Broomhead, D. B. Kell and M. R. H. White, *Science*, 2004, **306**, 704-708.
20. S. Tay, J. J. Hughey, T. K. Lee, T. Lipniacki, S. R. Quake and M. W. Covert, *Nature*, 2010, **466**, 267-271.
21. D. A. Turner, P. Paszek, D. J. Woodcock, D. E. Nelson, C. A. Horton, Y. Wang, D. G. Spiller, D. A. Rand, M. R. H. White and C. V. Harper, *J. Cell Science*, 2010.
22. L. M. Kingeter, S. Paul, S. K. Maynard, N. G. Cartwright and B. C. Schaefer, *J Immunol*, 2010, **185**, 4520-4524.
23. J. Bagnall, J. Leedale, S. E. Taylor, D. G. Spiller, M. R. White, K. J. Sharkey, R. N. Bearon and V. See, *The Journal of biological chemistry*, 2014, **289**, 5549-5564.
24. N. Yissachar, T. Sharar Fischler, A. A. Cohen, S. Reich-Zeliger, D. Russ, E. Shifrut, Z. Porat and N. Friedman, *Mol Cell*, 2013, **49**, 322-330.
25. N. C. Reich and L. Liu, *Nature reviews. Immunology*, 2006, **6**, 602-612.
26. F. Marangoni, T. T. Murooka, T. Manzo, E. Y. Kim, E. Carrizosa, N. M. Elpek and T. R. Mempel, *Immunity*, 2013, **38**, 237-249.
27. M.-H. Sung, N. Li, Q. Lao, R. A. Gottschalk, G. L. Hager and I. D. C. Fraser, *Switching of the Relative Dominance Between Feedback Mechanisms in Lipopolysaccharide-Induced NF-κB Signaling*, 2014.
28. G. K. Geiss, R. E. Bumgarner, B. Birditt, T. Dahl, N. Dowidar, D. L. Dunaway, H. P. Fell, S. Ferree, R. D. George, T. Grogan, J. J. James, M. Maysuria, J. D. Mitton, P. Oliveri, J. L. Osborn, T. Peng, A. L. Ratcliffe, P. J. Webster, E. H. Davidson, L. Hood and K. Dimitrov, *Nature biotechnology*, 2008, **26**, 317-325.
29. M. Batish, A. Raj and S. Tyagi, *Methods in molecular biology*, 2011, **714**, 3-13.
30. S. A. Kim, K. G. Heinze and P. Schwillie, *Nature methods*, 2007, **4**, 963-973.
31. C. Lois, E. J. Hong, S. Pease, E. J. Brown and D. Baltimore, *Science*, 2002, **295**, 868-872.
32. S. Sanjabi, K. J. Williams, S. Sacconi, L. Zhou, A. Hoffmann, G. Ghosh, S. Gerondakis, G. Natoli and S. T. Smale, *Genes & development*, 2005, **19**, 2138-2151.
33. H. Kuroda, R. H. Kutner, N. G. Bazan and J. Reiser, *Journal of Virological Methods*, 2009, **157**, 113-121.
34. G. Rabut and J. Ellenberg, *Journal of microscopy*, 2004, **216**, 131-137.
35. H. Shen, G. Nelson, D. E. Nelson, S. Kennedy, D. G. Spiller, T. Griffiths, N. Paton, S. G. Oliver, M. R. White and D. B. Kell, *Journal of the Royal Society, Interface / the Royal Society*, 2006, **3**, 787-794.
36. C. J. Du, M. Marcello, D. G. Spiller, M. R. White and T. Bretschneider, *Cytometry. Part A : the journal of the International Society for Analytical Cytology*, 2010, **77**, 1137-1147.
37. T. Hubbard, D. Barker, E. Birney, G. Cameron, Y. Chen, L. Clark, T. Cox, J. Cuff, V. Curwen, T. Down, R. Durbin, E. Eyras, J. Gilbert, M. Hammond, L. Humniecki, A. Kasprzyk, H. Lehvaslaiho, P. Lijnzaad, C. Melsopp, E. Mongin, R. Pettett, M. Pocock, S. Potter, A. Rust, E. Schmidt, S. Searle, G. Slater, J. Smith, W. Spooner, A. Stabenau, J. Stalker, E. Stupka, A. Ureta-Vidal, I. Vastrik and M. Clamp, *Nucleic acids research*, 2002, **30**, 38-41.
38. C. Trapnell, L. Pachter and S. L. Salzberg, *Bioinformatics*, 2009, **25**, 1105-1111.
39. Y. Liao, G. K. Smyth and W. Shi, *Bioinformatics*, 2014, **30**, 923-930.
40. M. D. Robinson, D. J. McCarthy and G. K. Smyth, *Bioinformatics*, 2010, **26**, 139-140.
41. G. Dennis, Jr., B. T. Sherman, D. A. Hosack, J. Yang, W. Gao, H. C. Lane and R. A. Lempicki, *Genome biology*, 2003, **4**, P3.
42. F. Supek, M. Bosnjak, N. Skunca and T. Smuc, *PLoS one*, 2011, **6**, e21800.
43. N. Dross, C. Spriet, M. Zwerger, G. Muller, W. Waldeck and J. Langowski, *PLoS one*, 2009, **4**, e5041.
44. P. O. Gendron, F. Avaltroni and K. J. Wilkinson, *J Fluoresc*, 2008, **18**, 1093-1101.
45. Y. H. Foo, N. Naredi-Rainer, D. C. Lamb, S. Ahmed and T. Wohland, *Biophysical journal*, 2012, **102**, 1174-1183.
46. T. Dull, R. Zufferey, M. Kelly, R. J. Mandel, M. Nguyen, D. Trono and L. Naldini, *Journal of virology*, 1998, **72**, 8463-8471.
47. F. Katzen, *Expert opinion on drug discovery*, 2007, **2**, 571-589.
48. N. C. Shaner, P. A. Steinbach and R. Y. Tsien, *Nature methods*, 2005, **2**, 905-909.

## ARTICLE

49. R. Ando, H. Mizuno and A. Miyawaki, *Science*, 2004, **306**, 1370-1373.
50. D. M. Chudakov, S. Lukyanov and K. A. Lukyanov, *Nat. Protocols*, 2007, **2**, 2024-2032.
51. T. P. Hopp, K. S. Prickett, V. L. Price, R. T. Libby, C. J. March, D. Pat Cerretti, D. L. Urdal and P. J. Conlon, *Nat Biotech*, 1988, **6**, 1204-1210.
52. C. R. Raetz, C. M. Reynolds, M. S. Trent and R. E. Bishop, *Annual review of biochemistry*, 2007, **76**, 295-329.
53. B. Tian, D. E. Nowak and A. R. Brasier, *BMC genomics*, 2005, **6**, 137.
54. S. Hao and D. Baltimore, *Nature immunology*, 2009, **10**, 281-288.
55. G. Lahav, N. Rosenfeld, A. Sigal, N. Geva-Zatorsky, A. J. Levine, M. B. Elowitz and U. Alon, *Nature Genetics*, 2004, **36**, 147-150.
56. M. S. Hayden and S. Ghosh, *Cell*, 2008, **132**, 344-362.
57. P. Paszek, S. Ryan, L. Ashall, K. Sillitoe, C. V. Harper, D. G. Spiller, D. A. Rand and M. R. White, *Proc Natl Acad Sci U S A*, 2010, **107**, 11644-11649.
58. G. Natoli, *FEBS letters*, 2006, **580**, 2843-2849.
59. R. E. Lee, S. R. Walker, K. Savery, D. A. Frank and S. Gaudet, *Mol Cell*, 2014, **53**, 867-879.
60. J. Braunstein, S. Brutsaert, R. Olson and C. Schindler, *Journal of Biological Chemistry*, 2003, **278**, 34133-34140.
61. N. Soto-Nieves, I. Puga, B. T. Abe, S. Bandyopadhyay, I. Baine, A. Rao and F. Macian, *Journal of Experimental Medicine*, 2009, **206**, 867-876.
62. P. Chene, *Oncogene*, 2001, **20**, 2611-2617.
63. Y. Chen, J. D. Muller, P. T. So and E. Gratton, *Biophysical journal*, 1999, **77**, 553-567.
64. A. Kimura, T. Naka, T. Muta, O. Takeuchi, S. Akira, I. Kawase and T. Kishimoto, *P Natl Acad Sci USA*, 2005, **102**, 17089-17094.
65. H. B. Chi, S. P. Barry, R. J. Roth, J. J. Wu, E. A. Jones, A. M. Bennett and R. A. Flavell, *P Natl Acad Sci USA*, 2006, **103**, 2274-2279.
66. C. Farnier, S. Krief, M. Blache, F. Diot-Dupuy, G. Mory, P. Ferre and R. Bazin, *International journal of obesity and related metabolic disorders : journal of the International Association for the Study of Obesity*, 2003, **27**, 1178-1186.
67. S. P. Acebron, E. Karaulanov, B. S. Berger, Y. L. Huang and C. Niehrs, *Mol Cell*, 2014, **54**, 663-674.